



Cite this: *Dalton Trans.*, 2015, **44**, 20889

Hydrothermal synthesis of oxygen functionalized S–P codoped g-C₃N₄ nanorods with outstanding visible light activity under anoxic conditions

Shaozheng Hu,^{a,b} Lin Ma,^b Ying Xie,^b Fayun Li,^b Zhiping Fan,^b Fei Wang,^b Qiong Wang,^b Yanjuan Wang,^b Xiaoxue Kang^b and Guang Wu^{*a}

Extending the application of photocatalytic oxidation technology to the anoxic removal of organic pollutants that exist under some oxygen-free conditions is attractive but challenging. In this study, oxygen functionalized S–P codoped g-C₃N₄ nanorods with outstanding visible light activity under anoxic conditions are synthesized using a hydrothermal post-treatment. S and P codoping inhibits the crystal growth of graphitic carbon nitride, enhances the S_{BET} , decreases the band gap energy, and increases the separation efficiency of photogenerated electrons and holes, which increases the anoxic photocatalytic RhB degradation constant by approximately 6.5 times. Oxygen functionalization not only increases the adsorption ability of graphitic carbon nitride but also captures the photogenerated electrons to produce photogenerated holes for RhB degradation under anoxic conditions, leading to a doubling of the RhB degradation constant. This study provides new insight into the design and fabrication of anoxic photocatalysts.

Received 15th October 2015,
Accepted 4th November 2015

DOI: 10.1039/c5dt04035c

www.rsc.org/dalton

Introduction

Recently, the growing awareness of the energy crisis and environmental protection has encouraged extensive investigation of new clean energy to replace traditional fossil fuels.¹ Solar energy for use as a clean energy has attracted much attention. Semiconductor photocatalysis has emerged as one of the most fascinating technologies for eliminating organic pollutants and converting solar energy.^{2,3} In general, a photocatalysis process requires the participation of molecular oxygen, which can generate reactive oxygen species by capturing electrons. However, oxygen is not available in many environments, such as petroleum-contaminated aquifers, oil reservoirs and deep sediments.⁴ These anoxic environments would suppress the ability of traditional photocatalysts. Therefore, the design and synthesis of novel photocatalysts for the anoxic photocatalytic process is required.

Graphitic carbon nitride (g-C₃N₄), which is the most stable allotrope of covalent carbon nitride, has been widely used as a novel metal-free visible light photocatalyst for organic pollutant degradation,⁵ water reduction and oxidation,⁶ CO₂

capture⁷ and organic synthesis.⁸ The tunable condensation degree and distinctive heptazine ring structure endow g-C₃N₄ with good physicochemical stability as well as a fascinating electronic structure and a medium band gap (2.7 eV).¹ However, the shortcomings of g-C₃N₄ are as obvious as its advantages and include a low visible light utilization efficiency, small specific surface area and rapid recombination of the photogenerated electron–hole pairs. To advance this promising photocatalyst, many strategies have been applied, such as metal and non-metal doping,^{9–11} copolymerization,¹² semiconductor coupling¹³ and nanostructured design.¹⁴

Among these strategies, doping is one of the most effective and convenient methods. Noble metals, which act as effective electron captors, can improve the separation rate of photogenerated electrons and holes.¹¹ However, the high price of noble metals inhibits their practical application. Wang and our group^{15,16} determined that the optical and electronic properties of g-C₃N₄ could also be altered by transition metal doping such as Fe³⁺. Fe-doped g-C₃N₄ possesses a wider optical absorption range, leading to better photocatalytic performance. For non-metal doping, Zhang *et al.* first synthesized phosphorus doped g-C₃N₄ using dicyandiamide and the ionic liquid [Bmim]PF₆ as the raw material.⁹ The electrical conductivity and photocurrent were significantly improved after phosphorus doping. However, the ionic liquid [Bmim]PF₆ is not an ideal phosphorus source due to its high price and complicated synthesis process. More recently, our group synthesized phosphorus doped g-C₃N₄ using diammonium hydrogen phosphate

^aSchool of Chemistry and Materials Sciences, Heilongjiang University, Key Laboratory of Chemical Engineering Processes & Technology for High-efficiency Conversion (College of Heilongjiang Province), Harbin 150080, China.
E-mail: guangw001@163.com

^bCollege of Chemistry, Chemical Engineering, and Environmental Engineering, Liaoning Shihua University, Fushun 113001, China

as the raw material.¹⁷ The introduction of phosphorus increased the surface area, improved the visible light absorption and enhanced the separation efficiency of the photogenerated electrons and holes. *In situ* sulfur doping effectively enhanced the photocatalytic activities of g-C₃N₄. Hong *et al.* prepared mesoporous carbon nitride with *in situ* sulfur doping using thiourea as the raw material.¹⁸ The obtained catalyst exhibited a high quantum efficiency of 5.8% and was 30 times more active than native g-C₃N₄. Zhang *et al.* reported a facile sulfur-mediated approach to stimulate carbon nitride bulk condensation using amino group-free trithiocyanuric acid as the carbon nitride precursor.¹⁹ The texture, optical and electronic properties of the obtained catalyst were modified using this method. In addition to S and P, other dopants (halogen, C and B) have also been used.^{20–22} Codoping or tridoping could combine the advantages of these dopants, leading to improved photocatalytic performance. This approach has been widely used in TiO₂ modification.^{23–25} However, few studies concerning the preparation and properties of codoped g-C₃N₄ have been reported. In our previous study, the photocatalytic performance of the prepared Fe and P co-doped g-C₃N₄ was much higher than that of single doped g-C₃N₄.²⁶

Many properties of graphene or graphene oxide-related materials are closely related to the oxidation level of graphene.^{27,28} g-C₃N₄ has a structure and chemical properties similar to those of graphene. Therefore, the introduction of oxygen atoms into the g-C₃N₄ framework may affect the properties and photocatalytic performance. Although O-doped g-C₃N₄ has been successfully synthesized by Li and Dong,^{29,30} the use of hydrogen peroxide as an oxidant not only increases the cost but also makes tuning the oxidation level challenging. In this study, we synthesize oxygen functionalized S-P codoped g-C₃N₄ nanorods using a hydrothermal post-treatment in the absence of H₂O₂. The as-prepared oxygen functionalized S-P codoped g-C₃N₄ exhibits outstanding visible light activity under anoxic conditions. The effects of doping on the structural, optical and photocatalytic properties of the catalysts are discussed in detail.

Experimental

Preparation and characterization

In a typical experiment, 3 g of thiourea was dissolved in 15 ml of deionized water under stirring. Then, 0.06 g of (NH₄)₂HPO₄ was added. The obtained solution was heated to 100 °C to remove the water. The solid product was dried at 100 °C in an oven followed by milling and annealing at 520 °C for 2 h (at a rate of 5 °C min^{−1}). The prepared catalyst is referred to as P-SN. For comparison, two catalysts were prepared. The S doped g-C₃N₄ catalyst was prepared according to the same procedure mentioned above in the absence of (NH₄)₂HPO₄ and is referred to as SN. Neat g-C₃N₄ was prepared following the same procedure mentioned above using dicyandiamide as a raw material in the absence of (NH₄)₂HPO₄ and is referred to as CN. When dicyandiamide was used to replace thiourea fol-

lowing the same procedure as in the synthesis of P-SN, the obtained catalyst was denoted as P-CN.

The preparation procedure of the oxygen functionalized S-P codoped g-C₃N₄ nanorods was as follows: 0.5 g of the as-prepared P-SN was placed in a stainless autoclave, which has a 100 ml Teflon inner liner. 80 ml deionized water was added. The autoclave was sealed, placed in an oven, and maintained at 150 °C for 2, 6, 10 and 14 h. The solid was collected by centrifugation, washed with deionized water and dried at 80 °C. This material is referred to as P-SN(2 h), P-SN(6 h), P-SN(10 h) and P-SN(14 h).

The XRD patterns of the prepared samples were recorded on a Rigaku D/max-2400 instrument using Cu-K α radiation ($\lambda = 1.54 \text{ \AA}$). The scan rate, step size, voltage and current were 0.05° min^{−1}, 0.01°, 40 kV and 30 mA, respectively. Fourier transform infrared spectra (FT-IR) were obtained on a Nicolet 20DXB FT-IR spectrometer. Elemental analysis was performed by using a vario EL cube from Elementar Analysensysteme GmbH. The morphology of the prepared catalyst was observed by using a scanning electron microscope (SEM, JSM 5600LV, JEOL Ltd). UV-Vis spectroscopy was carried out on a JASCO V-550 model UV-Vis spectrophotometer using BaSO₄ as the reflectance sample. The XPS measurements were performed on a Thermo Escalab 250 XPS system with Al K α radiation as the excitation source. The binding energies were calibrated by referencing the C 1s peak (284.6 eV) to reduce the sample charge effect. For the Ar etching process, the sputtering chamber was filled with high purity Ar gas to $\sim 13 \text{ Pa}$. Pre-sputtering was performed for 30 min. After pre-sputtering, the samples were produced with a power of 50 W and $\sim 3 \text{ Pa}$ dynamic pressure of the Ar sputtering gas. Ar etching for 5 min at $\sim 1 \text{ nm min}^{-1}$ etching rate was performed to remove the surface layer of the sample. After being sputtered, the samples were moved directly into the XPS chamber in tightly closed XPS sample containers. Nitrogen adsorption was measured at $-196 \text{ }^{\circ}\text{C}$ on a Micromeritics 2010 analyser. All the samples were degassed at 393 K prior to the measurement. The BET surface area (S_{BET}) was calculated based on the adsorption isotherm. The water contact angle was measured at 25 °C using an OCA 20 contact angle system (Dataphysics, Germany). The photoluminescence (PL) spectra were measured at room temperature with a fluorospectrophotometer (FP-6300) using a Xe lamp as the excitation source. The electrochemical impedance spectra (EIS) were recorded using an EIS spectrometer (EC-Lab SP-150, BioLogic Science Instruments) in a three electrode cell by applying a 10 mV alternative signal *versus* the reference electrode (SCE) over a frequency range of 1 MHz to 100 mHz. The cyclic voltammograms were measured in a 0.1 M KCl solution containing 2.5 mM K₃[Fe(CN)₆]/K₄[Fe(CN)₆] (1 : 1) as a redox probe at a scanning rate of 20 mV s^{−1} in the same three electrode cell as the EIS measurement. The photocurrents were measured using an electrochemical analyser (CHI 618C Instruments) equipped with a rectangular shaped quartz reactor (20 × 40 × 50 mm) using a standard three electrode system. The prepared sample film was used as the working electrode, a Pt flake was used as the counter elec-

trode, and Ag/AgCl was used as the reference electrode. A 500 W Xe lamp was used to irradiate the working electrode from the back side. The light intensity on the working electrode was 120 mW cm^{-2} . In addition, a mechanical shutter was used to minimize the light exposure of the sample. A 1.0 M Na_2SO_4 solution was used as the electrolyte. The applied potential was 0.00 V vs. Ag/AgCl. All the measurements were performed at room temperature (298 K).

Photocatalytic reaction

RhB was selected as the model compound to evaluate the anoxic photocatalytic performance of the prepared $\text{g-C}_3\text{N}_4$ based catalysts in an aqueous solution under visible light irradiation. A total of 0.05 g of catalyst was dispersed in 200 ml of an aqueous solution containing RhB (10 ppm) in an ultrasound generator for 10 min. The suspension was transferred to a self-designed glass reactor and stirred for 30 min in the dark to achieve adsorption equilibrium. N_2 was continuously bubbled through the solution to remove O_2 during the reaction process. In the photoreaction under visible light irradiation, the suspension was exposed to a 250 W high-pressure sodium lamp with a main emission in the 400–800 nm range. The UV light portion of the sodium lamp was filtered by a 0.5 M NaNO_2 solution. All the runs were conducted at ambient pressure and 30 °C. At specific time intervals, 4 ml of the suspension was removed and immediately centrifuged to separate the liquid samples from the solid catalyst. The RhB concentrations before and after the reaction were measured using a UV-Vis spectrophotometer at a wavelength of 550 nm. The total organic carbon content (TOC) was measured using a TOC analyser (TOC-VCPH, Shimadzu).

Results and discussion

Fig. 1 shows the XRD patterns of the as-prepared $\text{g-C}_3\text{N}_4$ based catalysts. For CN, the peak at 13.1° corresponds to the in-plane structural packing motif of the tri-*s*-triazine units and is indexed as the (100) peak. The distance is calculated to be $d =$

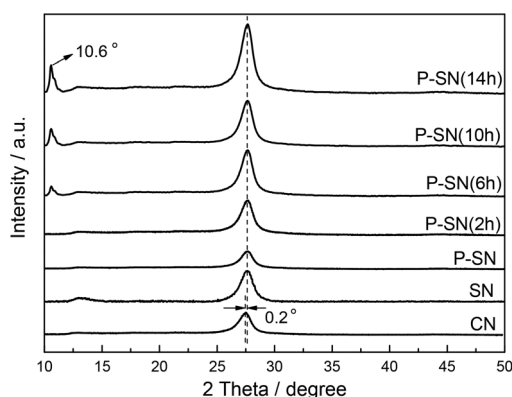


Fig. 1 XRD patterns of as-prepared $\text{g-C}_3\text{N}_4$ based catalysts.

0.67 nm. The peak at 27.50° corresponds to the interlayer stacking of the aromatic segments, with a distance of 0.324 nm, and is indexed as the (002) peak. The XRD peaks are shifted from 27.5° for CN to 27.7° for SN, corresponding to a decrease in the interplanar stacking distance from 0.324 to 0.322 nm. This result is most likely due to the S heteroatoms being doped into the $\text{g-C}_3\text{N}_4$ lattices, which disturbs the graphitic structure.^{19,31} For P-SN, the XRD peak position does not shift but the intensity decreases due to the P atoms being doped into the $\text{g-C}_3\text{N}_4$ lattices, inhibiting the crystal growth. This result is consistent with our previously reported result.¹⁷ After hydrothermal treatment, the peak intensity increases as the treatment time increases, indicating the growth of the $\text{g-C}_3\text{N}_4$ crystal. It is important to note that a new peak located at 10.6° was observed in P-SN(6 h) ($d = 0.83 \text{ nm}$). This peak has only been reported by Zhu *et al.*³² and is related to the hydrolysis/oxidation of $\text{g-C}_3\text{N}_4$, which lowers the polymerization degree of $\text{g-C}_3\text{N}_4$ and promotes the formation of a melem-like structure. During the hydrothermal treatment, the alignment of the tri-*s*-triazine units changes due to the hydrolysis/oxidation process. The partial dissociation of the tertiary amino group in the oxygen functionalized $\text{g-C}_3\text{N}_4$ gives rise to structures containing secondary amino and hydroxyl groups, which increases the unit cell length of the *c*-axis from 0.67 nm to 0.83 nm. A similar XRD peak at 10.6° has been observed for melem-containing materials.³³ The intensity of this signal increases as the hydrothermal treatment time increases, which indicates that the hydrolysis/oxidation of $\text{g-C}_3\text{N}_4$ occurs continuously during the hydrothermal process, leading to the formation of oxygen functionalized $\text{g-C}_3\text{N}_4$.

As shown in Table 1, SN and CN exhibit comparable S_{BET} . For P-CN and P-SN, this value increases to 15.2 and 17.8 $\text{m}^2 \text{g}^{-1}$, which is due to the P atoms being doped into the $\text{g-C}_3\text{N}_4$ lattices inhibiting the crystal growth. Along with the hydrothermal process, the S_{BET} of the as-prepared catalysts initially increases slightly for P-SN(2 h) and then quickly decreases. These trends are most likely due to the morphological changes of $\text{g-C}_3\text{N}_4$ during the hydrothermal process. The morphologies of the representative samples were examined by SEM analysis (Fig. 2). The results in Fig. 2a indicate that SN is composed of a large number of irregular particles. These particles exhibit a layered structure similar to that of the graphite analogue. In

Table 1 S_{BET} , C/N ratio, mass percentages of S, P and O, RhB adsorption percentages (A%) and rate constant (*k*) of the as-prepared catalysts

Catalyst	S_{BET} ($\text{m}^2 \text{g}^{-1}$)	C/N ratio	S cont. (wt%)	P cont. (wt%)	O cont. (wt%)	A (%)	<i>k</i> (min^{-1})
CN	9.5	0.71	0	0	2.5	6	0.002
SN	9.2	0.69	0.82	0	2.6	8	0.0024
P-CN	15.2	0.69	0	1.3	2.4	5	0.002
P-SN	17.8	0.68	0.82	1.4	2.8	7	0.013
P-SN(2 h)	18.6	0.68	0.80	1.3	5.5	10	0.018
P-SN(6 h)	13.6	0.68	0.80	1.2	7.4	11	0.026
P-SN(10 h)	8.8	0.69	0.83	1.3	10.5	12	0.015
P-SN(14 h)	6.9	0.68	0.82	1.3	12.8	14	0.010

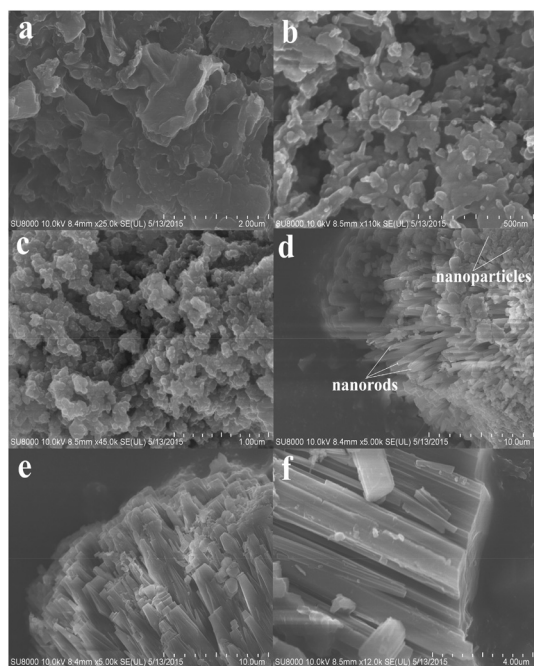


Fig. 2 SEM images of SN (a), P-SN (b), P-SN(2 h) (c), P-SN(6 h) (d), P-SN(10 h) (e) and P-SN(14 h) (f).

Fig. 2b, the size of the layered structure of P-SN decreased compared to that of SN, indicating that P doping inhibited the crystal growth of graphitic carbon nitride. This result is consistent with the XRD result. This smaller size corresponds to the greater S_{BET} of P-SN. After hydrothermal treatment for 2 h, the morphology changes from nanosheets to nanoparticles, as shown in Fig. 2c. When the hydrothermal time is increased to 6 h, these nanoparticles change to nanorods *via* self-assembly, which is accompanied by a substantial decrease in S_{BET} (Fig. 2d). A further increase in the hydrothermal time results in crystal growth of the $\text{g-C}_3\text{N}_4$ nanorods, leading to a further decrease in S_{BET} (Fig. 2e and f). Therefore, the morphology of the as-prepared $\text{g-C}_3\text{N}_4$ appears to be closely related to the degree of oxidation. Both SN and P-SN exhibit the typical sheet morphology of $\text{g-C}_3\text{N}_4$. After hydrothermal treatment, partial $\text{g-C}_3\text{N}_4$ is gradually hydrolysed to NH_3 and CO_3^{2-} . These $\text{g-C}_3\text{N}_4$ materials are exfoliated into small fragments, which are accompanied by morphology changes from nanosheets to nanoparticles. Then, these nanoparticles reassemble into nanorods as the hydrothermal treatment time increases. Therefore, the hydrothermal treatment has a significant influence on the morphology and oxidation level of $\text{g-C}_3\text{N}_4$, which most likely affects its photocatalytic performance. Interestingly, we treated the CN by a hydrothermal method. Only tiny CN was reserved after 2 h treatment. No solid was observed after 6 h treatment. For P-SN, after 14 h treatment, a small amount of the product P-SN(14 h) is still reserved. This indicates that doping probably plays an important role in the decomposition and reassembly process of carbon nitride.

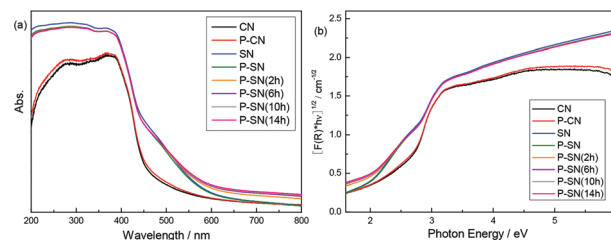


Fig. 3 UV-Vis spectra of the as-prepared $\text{g-C}_3\text{N}_4$ based catalysts.

UV-Vis spectra were recorded to investigate the electronic band structure of the as-prepared $\text{g-C}_3\text{N}_4$ based catalysts. The band gaps are estimated from the tangent lines in the plots of the square root of the Kubelka-Munk functions as a function of the photon energy.³⁴ As shown in Fig. 3a, the intensity of the absorbance of SN is higher than that of CN in the full spectrum. In comparison with CN, the absorption edge of SN is red shifted from 465 to 490 nm, corresponding to a decrease in the band gap energy from 2.65 to 2.53 eV, as shown in Fig. 3b. The red shift in the absorption wavelength indicates that the introduction of sulfur results in the absorption of more light energy to produce more photogenerated electron-hole pairs, which contributed to the improvement in the photoactivity of the catalysts. It is important to note that a broad absorption peak from 450 nm to 600 nm is observed for the SN. Wang *et al.* obtained a similar result and suggested that sulfur was most likely doped into the crystal lattice of $\text{g-C}_3\text{N}_4$, creating more defects.³⁵ Wang *et al.* simulated the total and partial DOS of pure and S-doped $\text{g-C}_3\text{N}_4$ using first principle calculations and suggested that the doped S atom influenced the distribution of C and N atoms in the lattice, leading to hybrid p orbitals among the C, N and S atoms and caused a broad absorption peak at 450–600 nm. In our previous work concerning P doped carbon nitride, we found that the visible light absorption of $\text{g-C}_3\text{N}_4$ increases slightly especially when the P concentration is lower than 2 wt%.¹⁷ From Table 1, it is shown that the P concentration of as-prepared catalysts is ~ 1.3 wt%. Thus it is reasonable that no obvious difference in light absorption is observed for P-CN compared with that of CN. As reported by Li *et al.*, the doping of oxygen into $\text{g-C}_3\text{N}_4$ decreased the band gap by 0.21 eV.²⁹ However, after hydrothermal treatment, the absorption in the 550–800 nm region slightly increases, but the absorption edge of the catalyst does not shift. This result suggests that oxygen functionalization, rather than O doping, occurs during the hydrothermal process.

The FT-IR spectra shown in Fig. 4 provide structural information for the as-prepared $\text{g-C}_3\text{N}_4$ based materials. For P-SN, a series of peaks in the 1200 to 1600 cm^{-1} range are attributed to the typical stretching modes of CN heterocycles, and the sharp peak located at 810 cm^{-1} is assigned to the bending vibrations of heptazine rings, which indicate that the synthesized $\text{g-C}_3\text{N}_4$ is composed of heptazine units. In our previous study, we reported the preparation of P doped $\text{g-C}_3\text{N}_4$

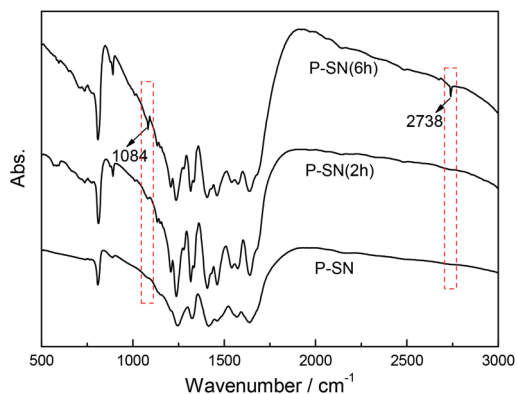


Fig. 4 FT-IR spectra of P-SN, P-SN(2 h) and P-SN(6 h).

using $(\text{NH}_4)_2\text{HPO}_4$ and dicyandiamide as raw materials.¹⁷ The peak centred at $ca.$ 950 cm^{-1} is observed in the as-prepared catalyst, which is assigned to the P–N stretching mode. However, the vibrations of the P-related group are not observed in this study, which is most likely due to the different raw material and low phosphorus content. A similar result was reported by Zhang *et al.*^{9,36} S-related vibrations are not observed for P-SN, which is consistent with previously reported results.^{19,35,37} For P-SN(2 h), all the characteristic vibrational peaks of $\text{g-C}_3\text{N}_4$ are observed, suggesting that the structure of $\text{g-C}_3\text{N}_4$ does not change. The O-related group is not clear due to the short hydrothermal time. For P-SN(6 h), in addition to the typical stretching modes of $\text{g-C}_3\text{N}_4$, two vibrations are observed at ~ 1084 and 2738 cm^{-1} . The peak at 1084 cm^{-1} is attributed to the stretching vibration of C–O, and the signals around 2730 cm^{-1} may be ascribed to the combination of the stretching and bending mode of C–O, which is typically related to the presence of carboxyl groups.

To confirm the structure of $\text{g-C}_3\text{N}_4$ and further identify the chemical state of the phosphorus, sulfur and oxygen elements, the $\text{g-C}_3\text{N}_4$ based catalysts were characterized using XPS. In Fig. 5a and b, the spectrum of $\text{g-C}_3\text{N}_4$ in both the N 1s and C 1s regions can be fitted with three contributions. For the C 1s region (Fig. 5a), the three contributions located at 284.6, 286 and 288.2 eV for CN are attributed to the sp^2 C atoms bonded to N in an aromatic ring (N-C=N), C=N or $\text{C}\equiv\text{N}$, which could be ascribed to defect-containing sp^2 hybridized carbon atoms present in graphitic domains, and pure graphitic sites in a CN matrix.^{38,39} In Fig. 5b, the three contributions of CN located at 398.4, 399.2 and 400.7 eV are assigned to the sp^2 hybridized aromatic nitrogen atoms bonded to carbon atoms (C-N=C), tertiary nitrogen N-(C)_3 groups linking structural motif or amino groups carrying hydrogen ($(\text{C})_2\text{-N-H}$) in connection with structural defects and incomplete condensation, and nitrogen atoms bonded to three carbon atoms in the aromatic cycles.⁴⁰ The spectra of SN and P-SN in the C 1s and N 1s regions do not exhibit a shift in the binding energy, which is consistent with previously reported results.³⁵ After hydrothermal treatment, the binding energy does not shift substantially, but a new peak is observed for P-SN(6 h) at $\sim 290\text{ eV}$ in

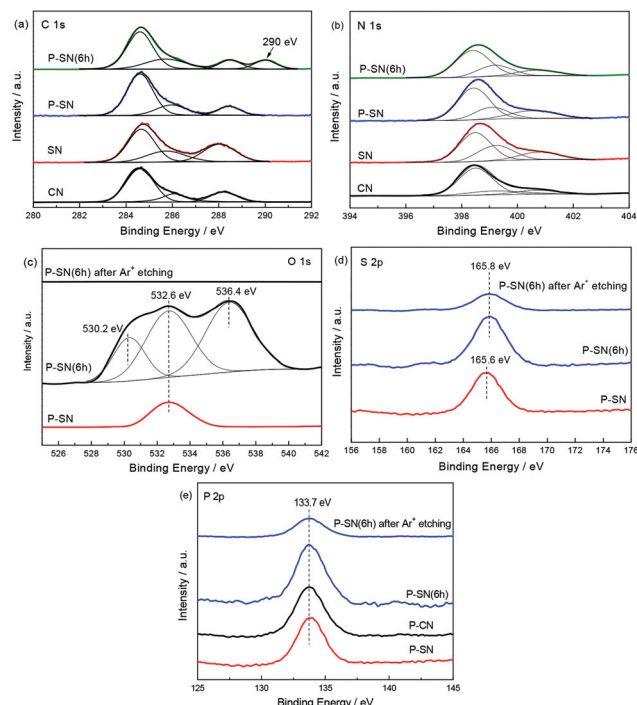


Fig. 5 XPS spectra of the as-prepared $\text{g-C}_3\text{N}_4$ based catalysts in the region of C 1s (a), N 1s (b), O 1s (c), S 2p (d) and P 2p (e).

Fig. 5a. This peak corresponds to general bonding between C and O, which can be in the form of O=C-O or C-O , implying the partial oxidation of C in $\text{g-C}_3\text{N}_4$.^{29,41}

In the O 1s region (Fig. 5c), the binding energy for P-SN is located at 532.6 eV, which corresponds to adsorbed H_2O or CO_2 . This result is a common phenomenon reported in previous studies.⁴² For P-SN(6 h), in addition to adsorbed H_2O or CO_2 , located at 532.6 eV, two additional peaks are observed. The binding energy located at 530.2 eV is attributed to the HO-C=O bond,⁴³ and the other peak, which has a high binding energy of 536.4 eV, most likely corresponds to a special form of C–OH on the catalyst surface.^{43,44} After Ar^+ etching, no peaks in the O 1s region remain for P-SN(6 h), indicating that surface oxygen functionalization occurred rather than oxygen doping of $\text{g-C}_3\text{N}_4$. In the S 2p region (Fig. 5d), the binding energy is located at 165.6 eV for P-SN. Chen *et al.* prepared S doped $\text{g-C}_3\text{N}_4$ and suggested that the binding energy at 163.9 eV was due to sulfur doping in the nitrogen position.⁴⁵ The higher binding energy obtained in this investigation suggests that sulfur can be doped into the carbon position instead of the nitrogen position to form a S–N bond. A similar result was reported by Wang *et al.*³⁵ After hydrothermal treatment, a 0.2 eV shift towards a higher binding energy is observed for P-SN(6 h), which is most likely due to S being oxidized to a certain degree after the introduction of oxygen atoms. The results in Fig. 5e indicate that the binding energies of P-CN, P-SN and P-SN(6 h) in the P 2p region are located at 133.7 eV, indicating the existing form of P is the same among the three catalysts. The P 2p binding ener-

gies of the P–N and P–C bonds are 133.5 eV and 131.5–132.5 eV, respectively.⁹ Therefore, phosphorus doping into the $g\text{-C}_3\text{N}_4$ lattice occurs in the form of a P–N bond. Besides, from the XPS results of P-SN(6 h) after Ar^+ etching, the S and P species still exist. The peak intensities for S and P are decreased compared with P-SN(6 h) but the binding energies are not shifted. This proves that S and P are doped into the crystal lattice of $g\text{-C}_3\text{N}_4$. Based on the XPS results, oxygen functionalized S–P codoped $g\text{-C}_3\text{N}_4$ is obtained.

As shown in Table 1, the C/N ratio is 0.69 for SN, which is lower than that of CN (0.71). This result suggests that sulfur species may act as leaving groups, mediating the condensation of the $g\text{-C}_3\text{N}_4$ polymer. P doping and hydrothermal treatment do not influence the C/N ratio. No difference in the mass percentages of S and P in as-prepared catalysts obtained by elemental analysis (EA) is observed ($\sim 0.8\%$ and $\sim 1.3\%$, Table 1). The mass percentage of O gradually increases as the hydrothermal treatment time increases, which indicates an increased oxidation level.

EIS and PL spectra are very useful tools for characterizing the charge-carrier migration, and these spectra were employed to further confirm the interfacial charge transfer effect of the as-prepared $g\text{-C}_3\text{N}_4$ based catalysts. As shown in Fig. 6a, P-SN exhibits a decreased arc radius compared to that of SN. In general, the radius of the arc in the EIS spectra reflects the reaction rate on the surface of the electrode.⁴⁶ This decreased arc radius on the EIS Nyquist plot indicates that more effective separation of photogenerated electron–hole pairs and faster interfacial charge transfer are occurring.⁴⁷ After hydrothermal treatment, the arc radius further decreases, indicating that the separation rate is further increased after oxygen functionalization. This is probably due to the fact that oxygen functional groups can capture photogenerated electrons which promote the separation rate. The arc radius follows the order P-SN(2 h) < P-SN(6 h) < P-SN(10 h) < P-SN(14 h), which is in contrast to the order of the surface area. Thus we presume that the surface area possibly plays a role in the charge separation efficiency. A higher surface area results in a shorter migration distance, which is possibly favourable for charge transfer from the bulk to the surface of the $g\text{-C}_3\text{N}_4$ material and leads to a higher separation rate. In general, at a lower PL intensity, the separation rate of the photogenerated electron–hole pairs is higher. In Fig. 6b, the broad PL band of SN is located at

approximately 465 nm, which corresponds to the band–band PL phenomenon with the energy of light approximately equal to the band gap of $g\text{-C}_3\text{N}_4$.³⁸ This band–band PL signal may be due to excitonic PL, which primarily results from $n\text{-}\pi^*$ electronic transitions involving lone pairs of the nitrogen atoms in $g\text{-C}_3\text{N}_4$.⁴⁸ For the P doped and hydrothermally treated catalysts, the shape of the curves is similar to that of SN. However, the peak intensities decrease substantially. This order in the degree of PL quenching is consistent with the arc radius shown in the EIS spectra, which confirms our result. This increased separation rate of the photogenerated electron–hole pairs in the oxygen functionalized S–P codoped $g\text{-C}_3\text{N}_4$ catalysts could improve the visible light utilization, which is beneficial to the photocatalytic performance.

The anoxic photocatalytic performance of the as-prepared catalysts was evaluated by studying the degradation of RhB, which has positively charged organic end groups, in the absence of oxygen (Fig. 7a). The pH of the RhB solutions is 6.1 during the anoxic photodegradation process. Due to a high recombination rate for the electrons and holes, CN exhibits a very low degradation rate ($\sim 15\%$) and reaction rate constant (0.002 min^{-1}), as shown in Table 1. P-CN shows slightly increased activity. For SN, the activity increases ($\sim 23\%$ and 0.003 min^{-1}). For P-SN, the anoxic photocatalytic performance further increases to 66% and 0.013 min^{-1} , which is 6.5 times higher than that of CN. It is shown in the UV-Vis spectra that S doping can promote the light adsorption ability of $g\text{-C}_3\text{N}_4$. The EIS and BET results indicate that the separation rate of electrons–holes and surface area are increased after P doping. It is known that there are three main factors that affect the photocatalytic performance of a catalyst. First of all, the light absorption ability determines how many electron–hole pairs can be formed in the optical excitation process. Secondly, the separation rate determines how many electron–hole pairs are really contributing in the photocatalytic process. Thirdly, the surface area determines how many reactants can be degraded at the same time. In this work, S and P codoping improves the three performances mentioned above simultaneously, thus leading to the higher activity. After hydrothermal treatment for 6 h, the rate constant further increases to 0.026 min^{-1} for P-SN(6 h), which is 2 and 13 times higher than that of P-SN and CN, respectively; 92% RhB was degraded in 120 min under anoxic conditions. The total organic carbon (TOC) was measured to investigate the mineralization ability of RhB under anoxic conditions (Fig. 7b). The mineralization ability of the as-prepared catalysts exhibits a trend similar to that of the degradation rate. P-SN(6 h) exhibits the highest mineralization rate of 47%. The degradation rate and mineralization ability of the catalyst decrease as the hydrothermal treatment time further increases. The characterization results indicate that hydrothermal treatment can further increase the separation efficiency of the photogenerated electrons and holes, which is beneficial to the activity. In addition, the treatment can increase the grain size and decrease the S_{BET} , which is detrimental to the photocatalytic performance. Therefore, to investigate the origin of the enhanced anoxic photoactivity, we compare the adsorption

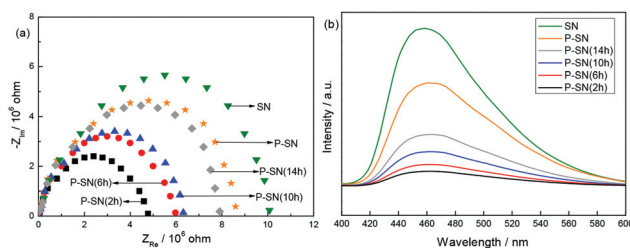


Fig. 6 EIS (a) and PL (b) spectra of the as-prepared $g\text{-C}_3\text{N}_4$ based catalysts.

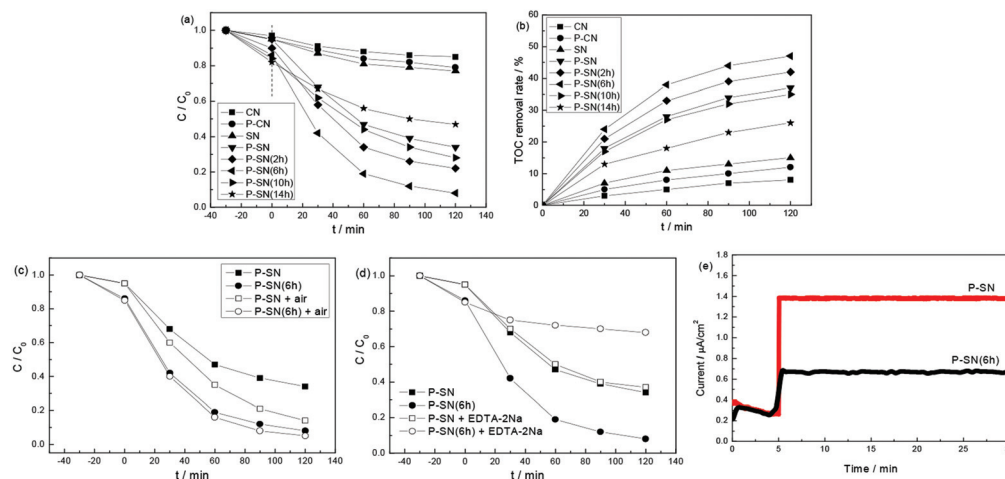


Fig. 7 Photocatalytic degradation and mineralization performance of RhB over the as-prepared catalysts under anoxic conditions (a–d) and photo-current responses of P-SN and P-SN(6 h) (e).

ability of the as-prepared $g\text{-C}_3\text{N}_4$ based catalysts under anoxic conditions. The adsorption of organic molecules onto the surface of a photocatalyst is critical to the photocatalytic process. As shown in Table 1, the adsorption ability (A) does not improve for the S and P doped $g\text{-C}_3\text{N}_4$ catalysts. After hydrothermal treatment, the adsorption ability increases as the treatment time increases. The adsorption property of the photocatalyst is related to its specific surface area (S_{BET}). The N_2 adsorption results shown in Table 1 indicate that the S_{BET} decreases substantially as the hydrothermal treatment time increases. This result indicates that the enhanced RhB adsorption ability may not be due to S_{BET} but to the effect of oxygen functionalization. Hydroxyl groups are hydrophilic, which not only favours the adsorption of hydrophilic organic molecules, such as RhB, but also improves the hydrophilicity of the photocatalyst.^{49,50} Therefore, the contact angle of water on the surface of P-SN and P-SN(6 h) was measured. The contact angle for P-SN is 66.8° , which is much larger than that for P-SN(6 h) (37.8°). The improved hydrophilicity of P-SN(6 h) further confirms the oxygen functionalization effect and explains its better adsorption ability. It is important to note that the adsorption ability increases from 7% for P-SN to 11% for P-SN(6 h), which has a growth rate much lower than that of the rate constant (k) (0.013 to 0.026 min^{-1}). Therefore, the enhanced anoxic RhB photocatalytic degradation performance is attributed not only to an improved adsorption ability but also to other more important factors related to oxygen functionalization.

The RhB photocatalytic degradation performance of P-SN and P-SN(6 h) was compared in the presence of oxygen (Fig. 7c). Air bubbling can substantially improve the RhB degradation over P-SN. However, the presence of oxygen does not substantially promote the photocatalytic RhB degradation rate over P-SN(6 h), indicating that molecular oxygen is crucial for the photocatalytic oxidation of RhB on P-SN but not necessary for P-SN(6 h). In addition, the depression effect of a hole

scavenger (EDTA-2Na) on the photocatalytic degradation of RhB over both catalysts under anoxic conditions was compared (Fig. 7d). The activity of P-SN decreases slightly after the addition of EDTA-2Na, and the rate constant of P-SN(6 h) decreases substantially from 0.026 to 0.005 min^{-1} . This result indicates that the photogenerated holes are responsible for RhB degradation under anoxic conditions. Typically, P-SN(6 h), which has a lower electron-hole recombination rate, would produce a higher photocurrent than P-SN. Therefore, the photocurrent responses of P-SN and P-SN(6 h) were measured (Fig. 7e). Surprisingly, the photocurrent generated on P-SN(6 h) is much lower than that on P-SN, which may be due to the photogenerated electrons being trapped by oxygen functional groups, decreasing the photocurrent over P-SN(6 h). In summary, based on the results shown in Fig. 7c–e, the oxygen functional groups can capture photogenerated electrons to produce photogenerated holes for RhB degradation under anoxic conditions.

In order to investigate the photocatalytic stability of oxygen functionalized S–P codoped $g\text{-C}_3\text{N}_4$, P-SN(6 h) was recycled three times. No obvious difference in S_{BET} , catalyst composition and anoxic RhB degradation rate is observed after three cycles, hinting its good stability (Table 2). To confirm the outstanding oxygen-free photocatalytic oxidation ability of the as-prepared oxygen functionalized S–P codoped $g\text{-C}_3\text{N}_4$, MO, MB, and phenol were used as organic pollutants. As shown in

Table 2 Comparison of S_{BET} , catalyst composition and anoxic RhB degradation rate ($D\%$) between fresh and reused P-SN(6 h)

Catalyst	S_{BET} ($\text{m}^2 \text{ g}^{-1}$)	C/N ratio	S cont. (wt%)	P cont. (wt%)	O cont. (wt%)	D (%)
Fresh P-SN(6 h)	13.6	0.68	0.80	1.2	7.4	92
Reused P-SN(6 h)	12.9	0.67	0.82	1.2	7.6	92

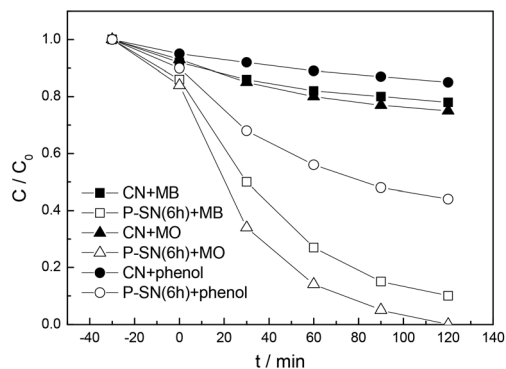


Fig. 8 MB, MO and phenol photocatalytic degradation performance over the as-prepared CN and P-SN(6 h) under anoxic conditions.

Fig. 8, P-SN(6 h) exhibits good photocatalytic degradation performance compared to CN. Therefore, this oxygen functionalized S-P codoped g-C₃N₄ can be widely used for the photocatalytic degradation of organic pollutants under anoxic conditions.

Conclusions

In summary, the oxygen functionalized S-P codoped g-C₃N₄ nanorods, which have outstanding visible light activity under anoxic conditions, are synthesized using a hydrothermal post-treatment. The XRD, UV-Vis, SEM, PL and EIS results indicate that S and P codoping inhibits the crystal growth of graphitic carbon nitride, enhances the S_{BET} , decreases the band gap energy and increases the separation efficiency of the photo-generated electrons and holes. Oxygen functionalization not only increases the adsorption ability of graphitic carbon nitride but also captures the photogenerated electrons to produce photogenerated holes for RhB degradation under anoxic conditions. P-SN(6 h) exhibits the highest RhB degradation constant (0.026 min^{-1}), which is 13 and 2 times higher than those of CN and P-SN. Not only RhB but also other organic pollutants (MO, MB, and phenol) can be degraded using this oxygen-free photocatalytic system. This study provides new insight into the design and fabrication of anoxic photocatalysts.

Acknowledgements

This work was supported by Science & Technology Research Foundation of Heilongjiang Province Education Bureau of China (no. 12541626), Postdoctoral Fund of Heilongjiang province of China (no. LBH-Z14208), Education Department of Liaoning Province (no. L2014145), Environmental Science and Engineering Innovation Team of Liaoning Shihua University ([2014]–11) and Students' Innovation Fund Project of China.

Notes and references

- 1 C. C. Chen, W. H. Ma and J. C. Zhao, *Chem. Soc. Rev.*, 2010, **39**, 4206.
- 2 G. Liu, L. Z. Wang, H. G. Yang, H. M. Cheng and G. Q. Lu, *J. Mater. Chem.*, 2010, **20**, 831.
- 3 D. Q. Zhang, G. S. Li and J. C. Yu, *J. Mater. Chem.*, 2010, **20**, 4529.
- 4 F. Widdel and R. Rabus, *Curr. Opin. Biotechnol.*, 2001, **12**, 259.
- 5 S. Z. Hu, F. Y. Li, Z. P. Fan, F. Wang, Y. F. Zhao and Z. B. Lv, *Dalton Trans.*, 2015, **44**, 1084.
- 6 X. C. Wang, K. Maeda, A. Thomas, K. Takanabe, G. Xin, J. M. Carlsson, K. Domen and M. Antonietti, *Nat. Mater.*, 2009, **8**, 76.
- 7 Q. F. Deng, L. Liu, X. Z. Lin, G. H. Du, Y. P. Liu and Z. Y. Yuan, *Chem. Eng. J.*, 2012, **203**, 63.
- 8 M. B. Ansari, H. L. Jin, M. N. Parvin and S. E. Park, *Catal. Today*, 2012, **185**, 211.
- 9 Y. J. Zhang, T. Mori, J. H. Ye and M. Antonietti, *J. Am. Chem. Soc.*, 2010, **132**, 6294.
- 10 Y. Y. Bu, Z. Y. Chen and W. B. Li, *Appl. Catal., B*, 2014, **144**, 622.
- 11 C. Chang, Y. Fu, M. Hu, C. Y. Wang, G. Q. Shan and L. Y. Zhu, *Appl. Catal., B*, 2013, **142–143**, 553.
- 12 J. S. Zhang, X. F. Chen, K. Takanabe, K. Maeda, K. Domen, J. D. Epping, X. Z. Fu, M. Antonietti and X. C. Wang, *Angew. Chem., Int. Ed.*, 2010, **49**, 441.
- 13 C. S. Pan, J. Xu, Y. J. Wang, D. Li and Y. F. Zhu, *Adv. Funct. Mater.*, 2012, **22**, 1518.
- 14 X. C. Wang, K. Maeda, X. F. Chen, K. Takanabe and K. Domen, *J. Am. Chem. Soc.*, 2009, **131**, 1680.
- 15 X. F. Chen, J. S. Zhang, X. Z. Fu, M. Antonietti and X. C. Wang, *J. Am. Chem. Soc.*, 2009, **131**, 11658.
- 16 S. Z. Hu, R. R. Jin, G. Lu, D. Liu and J. Z. Gui, *RSC Adv.*, 2014, **4**, 24863.
- 17 S. Z. Hu, L. Ma, J. G. You, F. Y. Li, Z. P. Fan, F. Wang, D. Liu and J. Z. Gui, *RSC Adv.*, 2014, **4**, 21657.
- 18 J. D. Hong, X. Y. Xia, Y. S. Wang and R. Xu, *J. Mater. Chem.*, 2012, **22**, 15006.
- 19 J. S. Zhang, J. H. Sun, K. Maeda, K. Domen, P. Liu, M. Antonietti, X. Z. Fu and X. C. Wang, *Energy Environ. Sci.*, 2011, **4**, 675.
- 20 G. G. Zhang, M. W. Zhang, X. X. Ye, X. Q. Qiu, S. Lin and X. C. Wang, *Adv. Mater.*, 2014, **26**, 805.
- 21 S. C. Yan, Z. S. Li and Z. G. Zou, *Langmuir*, 2010, **26**, 3894.
- 22 Y. P. Li, S. L. Wu, L. Y. Huang, J. L. Wang, H. Xu and H. M. Li, *Mater. Lett.*, 2014, **137**, 281.
- 23 X. Ding, X. Song, P. N. Li, Z. H. Ai and L. Z. Zhang, *J. Hazard. Mater.*, 2011, **190**, 604.
- 24 N. Patel, R. Jaiswal, T. Warang, G. Scardueli, A. Dashora, B. L. Ahuja, D. C. Kothari and A. Miotello, *Appl. Catal., B*, 2014, **150–151**, 74.
- 25 H. Q. Jiang, P. P. Yan, Q. F. Wang, S. Y. Zang, J. S. Li and Q. Y. Wang, *Chem. Eng. J.*, 2013, **215–216**, 348.

- 26 H. Q. Jiang, Q. Y. Wang, S. Y. Zang, J. S. Li and Q. F. Wang, *J. Hazard. Mater.*, 2013, **261**, 44.
- 27 Y. Zhu, S. Murali, W. Cai, X. Li, J. W. Suk, J. R. Potts and R. S. Ruoff, *Adv. Mater.*, 2010, **22**, 3906.
- 28 S. M. Tan, A. Ambrosi, C. K. Chua and M. Pumera, *J. Mater. Chem. A*, 2014, **2**, 10668.
- 29 J. H. Li, B. Shen, Z. H. Hong, B. Z. Lin, B. F. Gao and Y. L. Chen, *Chem. Commun.*, 2012, **48**, 12017.
- 30 G. H. Dong, Z. H. Ai and L. Z. Zhang, *RSC Adv.*, 2014, **4**, 5553.
- 31 J. D. Hong, X. Y. Xia, Y. S. Wang and R. Xu, *J. Mater. Chem.*, 2012, **22**, 15006.
- 32 X. Bai, L. Wang, R. Zong and Y. Zhu, *J. Phys. Chem. C*, 2013, **117**, 9952.
- 33 T. Sano, S. Tsutsui, K. Koike, T. Hirakawa, Y. Teramoto, N. Negishi and K. Takeuchi, *J. Mater. Chem. A*, 2013, **1**, 6489.
- 34 Y. I. Kim, S. J. Atherton, E. S. Brigham and T. E. Mallouk, *J. Phys. Chem.*, 1993, **97**(45), 11802.
- 35 K. Wang, Q. Li, B. S. Liu, B. Cheng, W. K. Ho and J. G. Yu, *Appl. Catal., B*, 2015, **176**, 44.
- 36 L. G. Zhang, X. F. Chen, J. Guan, Y. J. Jiang, T. G. Hou and X. D. Mu, *Mater. Res. Bull.*, 2013, **48**, 3485.
- 37 J. D. Hong, X. Y. Xia, Y. S. Wang and R. Xu, *J. Mater. Chem.*, 2012, **22**, 15006.
- 38 L. Ge and C. Han, *Appl. Catal., B*, 2012, **117–118**, 268.
- 39 W. Lei, D. Portehault, R. Dimova and M. Antonietti, *J. Am. Chem. Soc.*, 2011, **133**, 7121.
- 40 Y. W. Zhang, J. H. Liu, G. Wu and W. Chen, *Nanoscale*, 2012, **4**, 5300.
- 41 Y. Hou, Z. Wen, S. Cui, X. Guo and J. Chen, *Adv. Mater.*, 2013, **25**, 6291.
- 42 J. Mao, T. Peng, X. Zhang, K. Li, L. Ye and L. Zan, *Catal. Sci. Technol.*, 2013, **3**, 1253.
- 43 L. Wang, Y. Li, Z. Han, L. Chen, B. Qian, X. Jiang, J. Pinto and G. Yang, *J. Mater. Chem. A*, 2013, **1**, 8385.
- 44 L. Pedocchi, M. R. Ji, S. Lizzit, G. Comelli and G. Rovida, *J. Electron Spectrosc. Relat. Phenom.*, 1995, **76**, 383.
- 45 G. Liu, P. Niu, C. H. Sun, S. C. Smith, Z. G. Chen, G. Q. Lu and H. M. Cheng, *J. Am. Chem. Soc.*, 2010, **132**, 11642.
- 46 Y. Xu, H. Xu, L. Wang, J. Yan, H. Li, Y. Song, L. Huang and G. Cai, *Dalton Trans.*, 2013, **42**, 7604.
- 47 Q. W. Huang, S. Q. Tian, D. W. Zeng, X. X. Wang, W. L. Song, Y. Y. Li, W. Xiao and C. S. Xie, *ACS Catal.*, 2013, **3**, 1477.
- 48 V. N. Khabashesku, J. L. Zimmerman and J. L. Margrave, *Chem. Mater.*, 2000, **12**, 3264.
- 49 M. A. Gondal, X. F. Chang, M. A. Ali, Z. H. Yamani, Q. Zhou and G. B. Ji, *Appl. Catal., A*, 2011, **397**, 192.
- 50 K. Inumaru, M. Murashima, T. Kasahara and S. Yamanaka, *Appl. Catal., B*, 2004, **52**, 275.